The Astrophysical Journal, 727:51 (11pp), 2011 January 20 doi:10.1088/0004-637X/727/1/51

RED-SEQUENCE GALAXIES AT HIGH REDSHIFT BY THE COMBO-17+4 SURVEY

Marie-Hélène Nicol[1], Klaus Meisenheimer[1], Christian Wolf[1,2], and Christian Tapken[3]
[1] Max-Planck Institut für Astronomie, Königstuhl 17, D-69117 Heidelberg, Germany; nicol@mpia.de, meise@mpia.de
[2] Department of Physics, Denys Wilkinson Building, University of Oxford, Keble Road, Oxford OX1 3RH, UK; cwolf@astro.ox.ac.uk
[3] Astrophysikalisches Institut Potsdam, An der Sternwarte 16, D-14482 Potsdam, Germany; ctapken@aip.de
Received 2010 June 24; accepted 2010 November 15; published 2011 January 3

ABSTRACT

We investigate the evolution of the galaxy population since redshift 2 with a focus on the color bimodality and mass density of the red sequence. We obtain precise and reliable photometric redshifts up to $z = 2$ by supplementing the optical survey COMBO-17 with observations in four near-infrared bands on 0.2 deg^2 of the COMBO-17 A901-field. Our results are based on an H-band-selected catalog of 10,692 galaxies complete to $H = 21\overset{\text{m}}{.}7$. We measure the rest-frame color (U_{280}–V) of each galaxy, which across the redshift range of our interest requires no extrapolation and is robust against moderate redshift errors by staying clear of the 4000 Å break. We measure the color–magnitude relation of the red sequence as a function of look-back time from the peak in a color-error-weighted histogram, and thus trace the galaxy bimodality out to $z \simeq 1.65$. The (U_{280}–V) of the red sequence is found to evolve almost linearly with look-back time. At high redshift, we find massive galaxies in both the red and the blue population. Red-sequence galaxies with $\log M_*/M_\odot > 11$ increase in mass density by a factor of ∼4 from $z \sim 2$ to 1 and remain nearly constant at $z < 1$. However, some galaxies as massive as $\log M_*/M_\odot = 11.5$ are already in place at $z \sim 2$.

Key words: galaxies: evolution – galaxies: high-redshift – galaxies: photometry – galaxies: stellar content – surveys

Online-only material: color figures

1. INTRODUCTION

The lambda cold dark matter (ΛCDM) cosmological model predicts a bottom-up hierarchical scenario of structure formation in which large structures have been formed recently ($z \lesssim 1$) through mergers of existing smaller structures. It is still unclear when and how in this context galaxies have formed and how they have evolved into the baryonic structures made of stars we see today. The most evolved and massive systems known in the universe are found especially among red-sequence galaxies. They are straightforward to identify and seem to mark an end point in galaxy formation. Model predictions can thus be tested against measurements of the build-up of this population through cosmic time. To this end, the population needs to be tracked toward higher redshift. Their color, mass, and number density hold clues about their mass assembly over time.

It is still unknown when in the history of the universe the red-sequence population first emerged. Using the optical COMBO-17 data, Bell et al. (2004) have shown that the galaxy bimodality is present at all redshifts out to $z = 1$ and that the red sequence was already in place at $z = 1$ (see also Weiner et al. 2005). Several spectroscopic studies have observed massive red galaxies at $z \gtrsim 1.5$ (Cimatti et al. 2004; Glazebrook et al. 2004; Daddi et al. 2005; McGrath et al. 2007; Conselice et al. 2007; Kriek et al. 2008; Cassata et al. 2008), but did not allow the study of large samples. On the other hand, photometric redshift surveys combining optical and NIR data can provide photometric redshifts for larger samples of high redshift galaxies. Recently, Taylor et al. (2009) demonstrated the persistence of the red sequence up to $z \sim 1.3$ and Cirasuolo et al. (2007) as well as Franzetti et al. (2007) up to $z \sim 1.5$. Using color–color diagrams Williams et al. (2009) claimed the presence of quiescent galaxies analogous to a red sequence up to $z \sim 2$. A persistent issue for photometric redshift surveys is an increasing uncertainty in the measurement of rest-frame colors at high redshift ($z \gtrsim 1.5$). It increases the scatter in color–magnitude and color–stellar-mass diagrams, thus blurring the signature of a possible red sequence at high redshift. Especially, the expected small red-sequence population in field samples may be undetectable.

In this paper, we maximize the separation of red quiescent and blue star-forming galaxies by using the rest-frame color (U_{280}–V) as a diagnostic. Wolf et al. (2009) have shown how in galaxy clusters this color also tends to render star-forming red galaxies bluer to leave a more purified red sample. We use color-error-weighted histograms to improve the recognition of a red sequence in the face of increasing color uncertainties at high redshift (see Section 3 for all methods). In Section 4, we investigate the color distribution up to $z = 2$ and derive a color–magnitude relation (CMR) and a bimodality separation evolving with redshift. Thus, we attempt to estimate when the red-sequence population emerges. Ultimately, we quantify the evolution of the following galaxy properties: color, luminosity, mass, and number density for the red-sequence galaxy population since $z = 2$ (Section 5). We summarize and conclude this study in Section 6

Throughout this paper, we use the cosmological parameters $\Omega_m = 0.3$, $\Omega_\Lambda = 0.7$ and $H_0 = 70.7$ km s^{-1} Mpc^{-1}. All magnitudes are in the Vega system.

2. OBSERVATIONS

2.1. The COMBO-17+4 Survey

The COMBO-17+4 survey is the NIR extension of the optical COMBO-17 survey and is designed to probe galaxy evolution since $z = 2$. Near infrared data were necessary to obtain optical rest-frame properties for galaxies in the redshift range $1 < z < 2$, where the optical rest frame of galaxies is shifted into

Table 1
COMBO-17+4 Target Coordinates and Integration Times

Field[a]	R.A.	Decl.	Integration Time per Filter[b]			
			H	J_2	J_1	Y
	(J2000)	(J2000)	(ksec)	(ksec)	(ksec)	(ksec)
A901	**09h 56m 17s**	**−10° 01′25″**	**11.6**	**11.9**	**8.6**	**8.4**
A226	01h 39m 00s	−10° 11′00″	14.6	17.3	11.6	8.8
S11	11h 42m 58s	−01° 42′50″	16	4.5	8	10

Notes.
[a] Results in this paper are derived from the observations of the A901-field only.
[b] Integration time averaged over different subfields.

the NIR. The survey consists of observations in four NIR bands ($\lambda/\Delta\lambda$): the three medium bands $Y(1034/80)$, $J_1(1190/130)$, $J_2(1320/130)$, and the broadband $H(1650/300)$. In the long run, the COMBO-17+4 survey targets three independent fields (A901, A226, and S11) for a total coverage of 0.7 □° (see Table 1 for coordinates and integration times). The results derived in this paper are based on the observations of the A901-field only. This field contains the supercluster of galaxies A901/2 located at $z = 0.165$ where further multi-wavelength coverage from X-ray to radio was obtained by the STAGES survey (Gray et al. 2009).

2.2. Data

The NIR data were obtained in several observing runs from 2005 December to 2009 April with the NIR wide field camera Omega2000 at the prime focus of the 3.5 m telescope at Calar Alto Observatory in Spain. The camera has a pixel size of 0.″45 and a wide field of view of 15.′4 × 15.′4, so that a half-degree COMBO-17 field can be covered with a 2 × 2 mosaic. On the A901-field, only three of four pointings could be finished in the time awarded to the project, and hence the NIR data are missing in the south–west quadrant.

Also, an area of 68″ × 76″ centered at $(\alpha, \delta)_{J2000} = 09^h56^m32\overset{s}{.}4, -10°01'15''$ was cut out to avoid spurious objects created by the halo of a very bright ($K = 5\overset{m}{.}75$) Mira variable star, also known as the IRAS point source 09540−0946. The total NIR coverage is thus 690 □′ ≃ 0.19 □°. The optical data include a combination of 17 broad and medium bands centered between 365 nm and 915 nm and were obtained with the Wide Field Imager (WFI) at La Silla Observatory between 1999 February and 2001 January by the COMBO-17 survey (Wolf et al. 2003; Gray et al. 2009).

2.3. Data Analysis

The NIR data reduction and photometry were performed using the software ESO-MIDAS in combination with the *MPIAPHOT* package developed by Röser & Meisenheimer (1991) and the *OMEGA2k* data reduction pipeline developed by Faßbender (2003). The image data reduction consisted of flat fielding, dark current, and sky background subtraction as well as correction for bad pixels and pixel hits by cosmic ray events. Additive stray light appearing in a ring shape in all scientific and calibration images taken with the Omega2000 camera have been subtracted at the flat-field level for images taken in the Y, J_1, and J_2 filters where the stray light, if not corrected, would have contributed an additive 5%, 5%, and 10% to the flux, respectively. No stray light correction has been done for the H-band images where the additive contribution is negligible at <0.5%.

From the co-added H-band images of the three pointings we created an H-band mosaic image with a total exposure time of 11600 s pixel^{-1} and 1.″03 seeing on average. The summation process assigned a weight to each input image according to its transmission, background noise and point-spread function (PSF), so that the H-band mosaic has an optimal PSF. Using SExtractor (Bertin & Arnouts 1996) with default parameters we obtained a deep H-band source catalog with 31,747 objects. The astrometry was performed with IRAF (Tody 1993) using hundreds of bright ($H \lesssim 16\overset{m}{.}0$) 2MASS point sources in common with our catalog reaching an accuracy of 0.″1 in R.A. and decl.

The optical photometry has been re-derived for the source positions in the H-band catalog instead of the previous R-band catalog. Hence, optical and NIR photometry in all 21 bands of the COMBO-17+4 survey are measured in apertures matched in location and in size. In practice, we use a Gaussian weighting function in our aperture to give more weight to the bright central parts of an object and less weight to the fainter outer parts. Using a Gaussian sampling function and assuming a Gaussian seeing PSF allows us to sample identical areas of an object independent of seeing: we adjust the width of the Gaussian aperture to counteract seeing changes such that the integral over the aperture is conserved under seeing changes. Mathematically, our brightness measurements are identical to placing apertures with a Gaussian weighting function of 1.″7 FWHM onto a seeing-free image in all bands (COMBO-17 chose 1.″5 given the slightly better seeing of its optical data). The NIR filters Y, J_1, J_2, and H reach 10σ aperture magnitude limits of $22\overset{m}{.}1$, $21\overset{m}{.}5$, $21\overset{m}{.}4$, and $21\overset{m}{.}0$, respectively.

The COMBO-17 spectrophotometric stars have been used to ensure the calibration of the optical bands between each other (Wolf et al. 2001). We extended the calibration into the NIR using the Pickles (1998) spectral library by visually matching the colors of point sources in our data to main sequence stars in the library. We estimate that the relative calibration between optical and NIR has a limited accuracy on the order of 7%. The calibration of our photometry in the H-, J_2-, and J_1-bands has been verified by comparing the H magnitude and the average value of the J_2 and J_1 magnitude respectively to the H and J magnitudes of 340 stars with $H \lesssim 16$ in common with the 2MASS catalog. For the point sources, we found a mean offset in magnitude of < 1% in the H band and <0.4% in the averaged J_1- and J_2-bands. No verification could be done for the Y-band magnitude since no point-source catalog currently exists in this waveband.

3. METHODS

3.1. Photometric Classification and Redshifts

Photometric redshifts were determined using the multi-color classification code by Wolf (1998) as it was done in COMBO-17. Objects are divided into the four classes star, white dwarf, galaxy and quasar by comparing measured colors with color libraries calculated from spectral templates. The templates for stars and quasars are identical to those in Wolf et al. (2004), while a modified library has been built for galaxies, in order to allow reliable estimates of the stellar mass (see below). At the bright end, the redshift accuracy is limited by systematic errors in the relative calibration of the different wavebands or in a mismatch between templates and observed spectra. At the faint end, photon noise dominates.

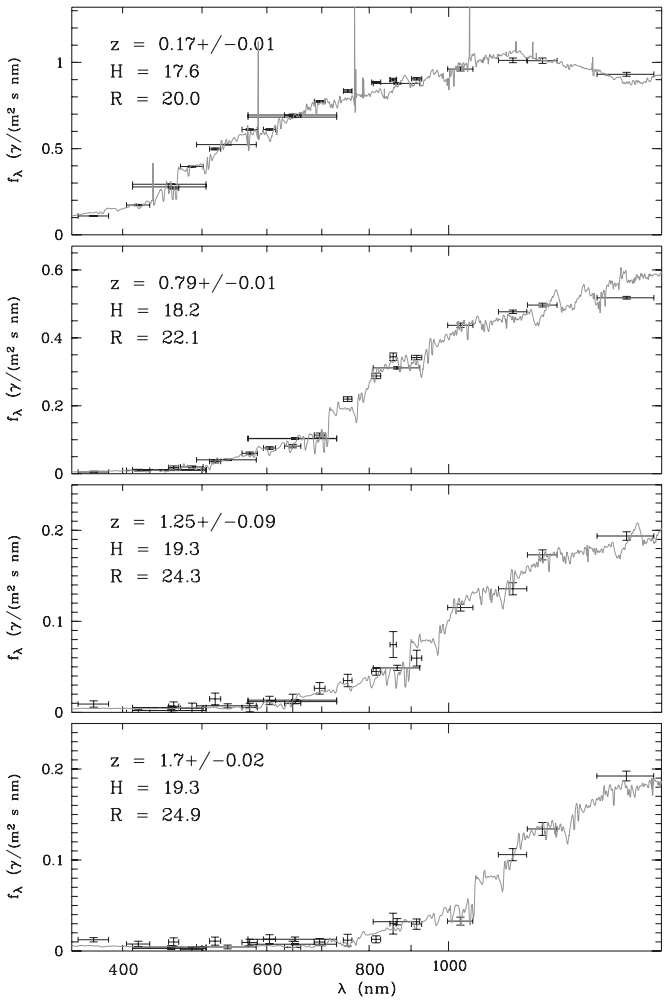

Figure 1. Spectral energy distributions of four red-sequence galaxies at different redshifts.

This data set is a superset of the COMBO-17 data with the four NIR bands added. As a result, the photo-z's have changed very little at $z < 1$, where the NIR bands add little constraints, but it is reasonable to assume that they have improved over the optical-only results at $z > 1$. In Figure 1, we show four examples of red galaxy spectral energy distributions (SEDs) and their best-fit templates. At $z < 1$, the fit is clearly constrained by the original COMBO-17 data at $\lambda < 1\mu$ m. At $z > 1$, the four NIR bands act in concert with the optical data, while for red galaxies toward $z = 2$ they are the sole providers of significant flux detections. The two $z > 1$ galaxies shown are examples of EROs with $R - H \sim 5$ and 5.7, respectively. To the eye, their redshift is clearly constrained by locating the break between neighboring pairs of filters, while the fit takes all filters into account to constrain the redshift further.

COMBO-17 photo-z's have been shown to be accurate to $\sigma_z/(1+z) < 0.01$ at $R < 21$, < 0.02 at $R < 23$ (Wolf et al. 2004), albeit on a different field (the CDFS). On the A901 and S11 field, we only have spectra for galaxies at $z < 0.3$. From these, the photo-z dispersion of the cluster A901/2 has been measured as 0.005 rms (Wolf et al. 2005; Gray et al. 2009). Presently, we lack the ability to confirm our photo-z's at $z > 1$ here. Hence, we need to rely on the plausibility of the SED fits to the photometry as shown in Figure 1.

However, the photometric errors and the grid of templates allow the estimation of probability distributions and confidence

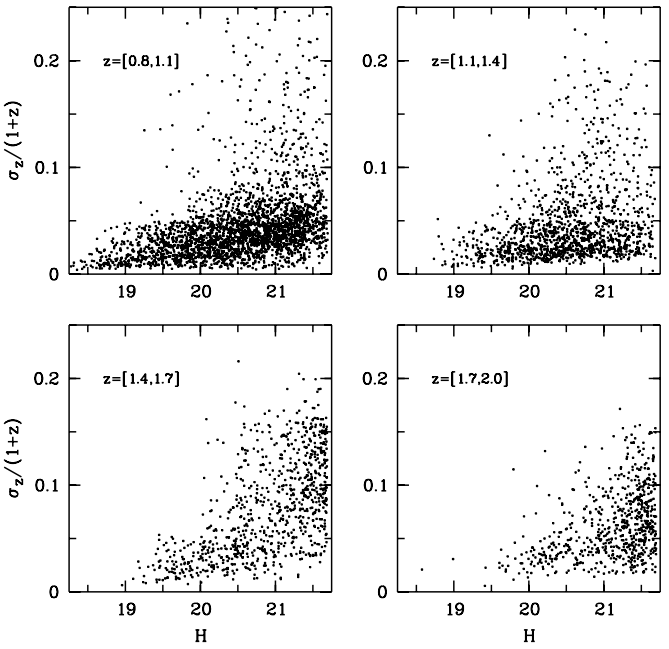

Figure 2. Photometric redshift accuracy H-band magnitude in higher-z redshift intervals.

intervals in redshift for each galaxy. These estimated redshift errors are shown in Figure 2, where they illustrate the change in behavior with redshift and magnitude. Obviously, photometric errors increase toward faint magnitudes and propagate into redshift errors, but at $z < 1.2$ the redshift error is still very much driven by the deep optical photometry. Hence, the bulk of objects have $\sigma_z/(1+z) < 0.05$ even at our adopted H-band limit. At $z > 1.2$, however, where the main redshift constraints are in the NIR bands, a clear upswing of redshift errors with H-band magnitude can be seen.

3.2. Galaxy Samples

After eliminating ∼2300 objects classified as non-galaxies, we defined our sample by first applying an H-band selection above our 5σ detection limit of $H = 21\overset{\text{m}}{.}7$. However, we are concerned with the evolution of galaxy samples that need to be complete in rest-frame V-band luminosity or stellar masses. We avoid a color bias by applying further magnitude cuts and eliminate from our color–magnitude diagrams (CMDs) those faint tails of the galaxy distribution that are known to be incomplete. Across our redshift range several observed bands with different completeness limits map onto the rest-frame V band. Hence, we opted to apply the following two further cuts.

(1) At $z < 0.43$, the entire observed R-band is redward of the 4000 Å-break and roughly coincides with the rest-frame V band. Here, we require galaxies to have $R < 23\overset{\text{m}}{.}5$, which is the completeness limit of the optical-only COMBO-17 redshifts for $z < 0.43$ galaxies. The presence of NIR data may have deepened our completeness in this regime, but we opt to err on the conservative side and eliminate this faint end from our analysis. Note that optically faint red galaxies at higher redshift (such as EROs) are by definition NIR-bright and thus have very well-constrained SED fits and (higher) redshift estimates (see Figure 1).

(2) In the redshift range $0.43 < z < 1.4$, the Y band is redward of the break and we require $Y < 22\overset{\text{m}}{.}8$ (our 5σ-limit). Again, objects that are particularly red in $Y - H$ are expected to reside at $z > 1.4$.

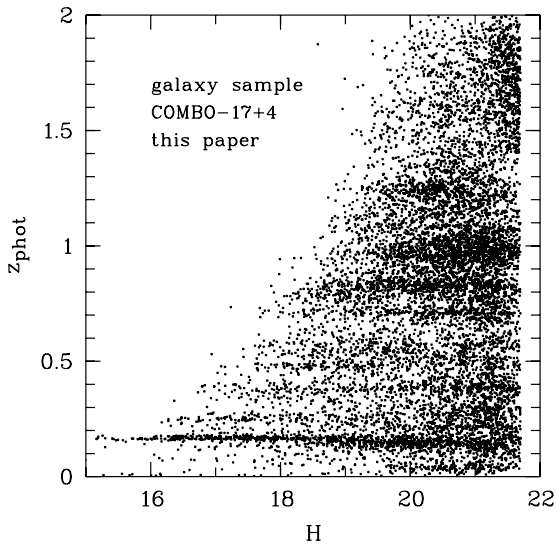

Figure 3. Photometric redshift distribution of our galaxy sample vs. *H*-band magnitude.

Finally, at $z > 1.4$ the SED around the 4000 Å break is entirely sampled by our NIR filters and the $H < 21\overset{m}{.}7$ selection is sufficient to ensure completeness and an accurate redshift estimate. These selections are complete in stellar mass $\log(M_*/M_\odot)$ to 8.5, 9.5, and 10 in the redshift ranges $z < 0.43$, $0.43 < z < 1.4$, and $z > 1.4$, respectively.

After removing galaxies with bad flags, our sample contains 10,692 galaxies. Figure 3 shows this sample and reveals already a number of large-scale structures. The dominant overdensity at $z \sim 0.16$ is the original main target of this COMBO-17 field, the supercluster region A901/2 with well over 1000 galaxies. Further clusters and large-scale structures have been identified and reported in this field, partly from weak gravitational lensing (Taylor et al. 2004; Simon et al. 2010) and partly from a galaxy cluster search (Falter et al. 2010). These include localized clusters embedded in large-scale structures at $z \sim 0.26, 0.37, 0.5, 0.7, 0.8$. At higher redshift and fainter magnitudes, i.e., $z > 0.8$ and $H > 20$, redshift focusing effects are possible, and structures which appear only at faint magnitudes but without a sharp tail to the bright edge are unlikely to be physically localized overdensities. In Figure 3, the two possible unreal overdensities are the faint-end blobs at $z \sim 1$ and $z \sim 1.2$. Their appearance does not require redshift errors in excess of what is discussed above, but only a mild focusing within the allowed errors. At $z > 1.2$, no structure can be seen, as any physical contrast has been smoothed by our redshift errors.

The histogram of photometric redshifts of the complete galaxy sample is shown in Figure 4. Here, we show first the optical-only COMBO-17 redshifts of four different fields, which demonstrate the signature of abundant large-scale structure. In the case of the CDFS, these have been reported consistently by a variety of groups. Overall, the structures include six Abell clusters as well as further clusters and rich groups, usually characterized by a pronounced red sequence. It is thus clear that we investigate a variety of environments across redshift, and only the combination of several fields will eventually suppress error propagation from field-to-field variation.

The histogram in the right panel shows new redshifts after including the NIR bands of COMBO-17+4. It is selected by combined apparent-magnitude cuts in the *R*, *Y*, and *H* bands, instead of the sole *R* band in the optical-only photo-*z*'s, and thus numbers at higher redshifts are increased. The inclusion of NIR data allows for good photo-*z*'s at $z > 1$, but presently such data are only available for three quarters of the A901-field covering 0.2 □° area. This is our first look at $z > 1.2$ galaxies, while completion of our project will entail three fields with a different mix of environment at each redshift.

The bulk of our sample is in the range $0.7 < z < 1.1$, consistent with the $z = 0.9$ peak in the $n(z)$ found in COSMOS (Ilbert et al. 2010).

3.3. Spectral Library of Galaxies

The photometric redshifts of galaxies in the optical-only COMBO-17 (Wolf et al. 2004) are based on synthetic templates produced by the population synthesis model PEGASE (Fioc & Rocca-Volmerange 1997). A single, exponentially declining burst of star formation was assumed for the star formation history ($\tau = 1$ Gyr). The templates form a two-dimensional grid in which one parameter is the age since the start of the burst (60 steps between 0.05 to 15 Gyr) and the second one is extinction, which was modeled as a foreground screen of dust following the Small Magellanic Cloud (SMC) law defined by Pei (1992) in six steps from $A_V = 0$ to $A_V = 1.5$. Here, we employ a new library based on a two burst-model following the approach of Borch et al. (2006). The motivation for a two-burst model is to reproduce better the stellar population of blue galaxies that contain both an old stellar population and ongoing

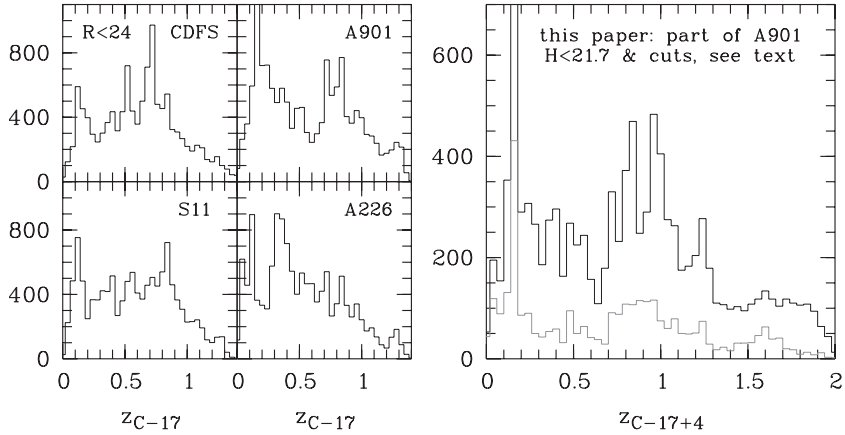

Figure 4. Left: original COMBO-17 photo-*z* distribution in four fields, illustrating field-to-field variation. Right: new COMBO-17+4 distribution of the sample used in this paper (black line), and the red sample as defined in Section 4.3 (gray line).

star formation activity and to provide more realistic mass-to-light ratios. However, the two-burst model by Borch et al. (2006) failed to deliver accurate redshifts.

Our new two-burst library solves this problem by including extinction again and adjusting the age and strength of the second burst. For red galaxies (ages > 3 Gyr) we leave the single-burst templates unchanged ($\tau_1 = 1$ Gyr), and for bluer galaxies we add a recent burst ($\tau_2 = 0.2$ Gyr) to the old population starting 2.75 Gyr after the first one. Increasingly blue galaxy templates are generated by both increasing the relative strength of the second burst *and* by moving the final age (at which the galaxy is observed) from 3.0 Gyr to 2.80 Gyr (i.e., toward the start of the second burst). This ensures that the templates fall into a region of the rest-frame color–color diagrams that is occupied by observed galaxies, and thus leads to very accurate photometric redshifts. We assume a Kroupa IMF, an initial metallicity of 0.01 ($\sim 2/3\, Z_\odot$) and neither infall nor outflow. More details will be given in K. Meisenheimer et al. (2011, in preparation).

3.4. Stellar Mass Estimation

The stellar mass of a galaxy is derived from the best-fitting template SED, whose characteristics are constrained mostly by the rest-frame spectrum between 280 nm and the V band, which is observed at all redshifts. Formally, we use data from all bands, but our masses can be seen to be derived from a galaxy's observed V-band luminosity and the V-band mass-to-light ratio of its best-fitting template.

Our use of a fixed rest-frame band to determine a galaxy's luminosity differs from that of Borch et al. (2006) who only used the reddest observed-frame band with good photometry, and thus may suffer unintended bias trends with redshift. At low redshifts $z < 0.5$, Borch et al. (2006) sample the rest-frame V band as well so that our mass estimate should only differ from theirs due to the different templates. Only due to the NIR extension in COMBO-17+4 can we continue to use the rest-frame V band out to $z = 2$.

Indeed, a comparison of galaxies at the redshift of the supercluster A901/2 ($0.150 < z < 0.175$) shows that systematic differences in the stellar masses do not exceed 0.1 dex. Beyond $z = 0.5$ the stellar masses derived here are superior due to the NIR photometry. We estimate a typical mass accuracy on the order of 30% across all redshifts.

We wish to assess possible biases in the stellar mass estimates arising from dust and consider the Bell & deJong (2001) equation,

$$\log_{10} M_*/M_\odot \propto -0.4 M_V + 1.305(B - V), \qquad (1)$$

because it allows an analytic derivation of a reddening vector in color–mass diagrams, and our masses are consistent with Equation (1) within ± 0.1 dex. Any dust reddening can now be seen as a mean reddening plus some structure. Approximating the mean reddening by a uniform screen of dust right in front of the stellar population changes its color by $\Delta(B - V) = E_{B-V}$ and its V-band luminosity by $\Delta V = R_V E_{B-V}$. The reddening-induced overestimate of the M/L ratio and the absorption-induced underestimate of L cancel exactly, if

$$0.4 R_V E_{B-V} = 1.305 E_{B-V} \rightarrow R_V = 3.2625, \qquad (2)$$

which is almost true for the Milky Way, LMC, or SMC dust law from Pei (1992). Dust acting like a foreground screen on the stellar population will thus not bias the mass estimates at all. However, if pockets of highly absorbed stars exist as well, they will be entirely withdrawn from the optical view and not contribute to either luminosity or color. They will thus be plainly not taken into account and the final mass estimate will be underestimated by just the stellar mass present in highly obscured pockets.

3.5. Rest-frame Luminosities and Colors

Rest-frame luminosities are derived from the observed photometry covering the wavelength range from the U band to the H band. We obtained rest-frame luminosities for the V band in the Johnson photometric system as well as for the U_{280} band, a synthetic UV continuum band with a top-hat transmission curve that is centered at $\lambda = 280$ nm and 40 nm wide. These two filters are covered by our observed bands across almost the entire range of interest. This is essential as our study does not rely on SED extrapolation except for galaxies in the small range $0.2 < z < 0.3$. The rest-frame color U_{280}–V is measured robustly against redshift errors since both filters are located in smooth continuum regions of the galaxy spectra. The Johnson U band, in contrast, partly overlaps with the 4000 Å break and is hence affected strongly by small uncertainties in the redshift determination.

The rest-frame luminosities are derived as described by Wolf et al. (2004). The best-fitting SED is placed into the aperture photometry and integrated over the redshifted rest-frame bands. We have taken into account the interstellar foreground extinction as well as a correction from aperture to total photometry, which could be biased by color gradients. It is determined from the total magnitude MAG-BEST derived by SExtractor on the H-band image and thus certainly correct for any rest-frame band overlapping with the observed H band. The magnitude errors are determined from a propagation of photometric errors. They include a minimum error of $0\overset{\mathrm{m}}{.}1$ to take into account redshift errors and overall calibration uncertainties, for details see Wolf et al. (2004).

3.6. Error-weighted Color Histograms

Generally, color and magnitude information can be used to separate passive red galaxies from star-forming blue ones. However, at high redshift the well-known color bimodality may be blurred by scatter from relatively large errors on the color measurements. We try to manage this challenge and investigate the galaxy color bimodality through cosmic time by using error-weighted color histograms. This method represents each galaxy by its Gaussian probability distribution in color c, i.e., $p(c) \sim e^{-(c-c_0)^2/2\sigma_c^2}$, where σ_c is the color error and p is normalized so that $\int p dc = 1$. Thus, a galaxy with a small error has a more peaked distribution and contributes more structure to the summed distribution than a galaxy with a large error. As a result, the structure in our histograms is driven entirely by galaxies with small color errors, while objects with large errors lift the overall counts without producing peaks. We produced error-weighted color histograms by summing all the Gaussian distributions within many thin redshift slices ($\Delta z \sim 0.1$) stepping through our full redshift range of $0 < z < 2$. Toward highest redshifts, the increasing color errors will dilute the contrast of the red-sequence peak. Redshift errors can also lead to some spill-over from a physical redshift bin into neighboring photo-z bins and produce scatter in our measured color evolution from bin to bin in redshift.

To better disentangle the red sequence from the blue cloud we have tilted the $(U_{280} - V)$ color in the color–magnitude plane, see

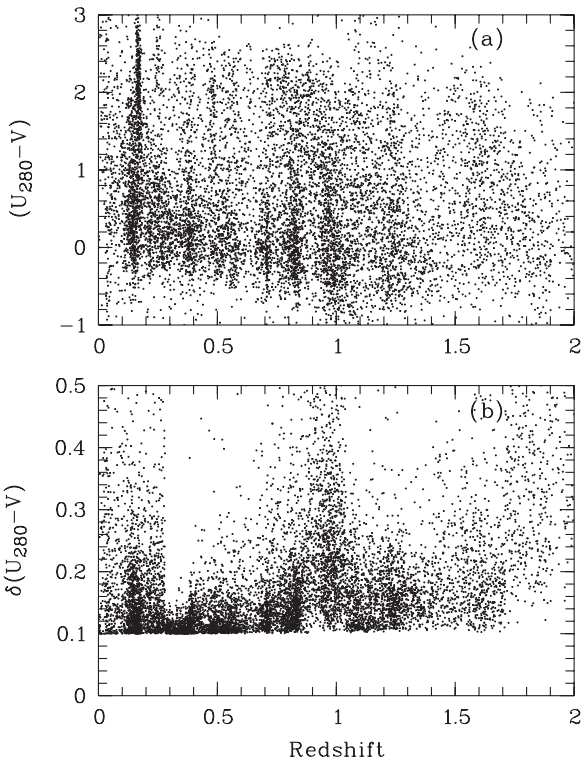

Figure 5. (a) Rest-frame color $(U_{280}–V)$ over redshift. The A901/2 supercluster produces a prominent feature at $z = 0.165$. (b) Color error over redshift, as determined from error propagation. At high redshift the color determination is less accurate, especially at $z \gtrsim 1.5$. An error floor of $0^{\rm m}.1$ is assumed, see Section 3.5.

Equation (3). The measured $(U_{280}–V)$ of each individual galaxy is projected along the slope of the red sequence as determined in the CMD of the supercluster A901/2 (see Figure 8, top left) to the pivotal magnitude $M_V = -20$:

$$(U_{280}–V)_{M_V=-20} = (U_{280} - V) + 0.3(M_V + 20). \quad (3)$$

The derived slope of 0.3 is consistent with that of 0.08 in the $(U - V)$ color in Bell et al. (2004).

4. EVOLUTION OF THE COLOR BIMODALITY

4.1. Rest-frame Colors and Color Errors as a Function of Redshift

Scatter in measured galaxy colors affects the appearance of the color bimodality in a CMD and may render it invisible, especially in a sample of low-density field galaxies where no clusters rich in red galaxies produce a well-defined sequence. As the scatter in color increases with redshift, this effect can prevent us from detecting a physically present high-redshift bimodality.

For a first assessment of our ability to trace bimodality, we plot the rest-frame $(U_{280}–V)$ color and its error $\delta(U_{280}–V)$ as a function of redshift in Figure 5. In panel (a), we see the number of red galaxies decreasing with redshift. Also, a lack of star-forming blue galaxies with $(U_{280}–V) < 1$ at $z > 1.5$ is caused by a red-object bias from our H-band-selected catalog. Panel (b) shows that the color accuracy is very good for objects located at low redshift $z \lesssim 0.9$. The bulk of the galaxies have a color error close to the assumed minimum of $0^{\rm m}.1$. The large scatter around $z \sim 1$ is caused by a locally increased magnitude error in the rest-frame V band that results from M_V being calculated from the relatively shallow narrowband J_1. In contrast, the U_{280} filter overlaps with the ∼3 mag deeper R band at $z \sim 1$. At $z > 1.7$, the color uncertainties grow larger again since the rest frame where the U_{280} band falls into the I band, which is our shallowest broadband.

4.2. Color Bimodality and the Emergence of the Red Sequence

In Figure 6, we plot error-weighted color histograms of galaxies in different redshift slices. Each panel shows two distinct peaks due to the bimodality, whereby the right peak represents red-sequence galaxies sitting on top of a tail of blue cloud galaxies reaching smoothly toward the red due to lower star formation rates or dust reddening. Clearly, a red galaxy sample defined by a color cut will comprise both quiescent red-sequence galaxies as well as dusty star-forming galaxies. At high redshift, we are unable to separate old red from dusty red galaxies, and so a red galaxy sample overestimates the space density of quiescent galaxies. However, the CMR should be well constrained, as only galaxies from the proper quiescent red sequence are focussed in color and contribute to the peak in the color histogram, while dusty red galaxies form a smooth underlying continuum spreading across the red-sequence and extending beyond.

The supercluster A901/2 seen in the top left panel has a particularly clear red sequence. Our results show a clear galaxy bimodality at $z < 1$ as already established by Bell et al. (2004). However, the depth of our survey allows us to extend the detection of the galaxy bimodality up to $z \sim 1.65$, the mean redshift of the highest interval where we can still detect two distinct distribution peaks. Beyond $z \sim 1.65$ it is not possible to confirm a galaxy color bimodality since the number of objects available for our analysis drops considerably. Figure 6 (bottom right) shows the distribution of 423 galaxies in the redshift interval $1.7 < z < 2$. It is clearly not bimodal, though this does not mean that the red sequence does not exist there. Our redshift errors are unlikely to be the main source of this disappearance, since the redshift error $\sigma_z/(1 + z)$ of luminous red galaxies with $M_V = [-23.5, -22]$ degrades only from a median value of ∼0.01 at $z = 0.8$ over ∼0.025 at $z = 1.2$ to ∼0.04 at $z = 1.6$. Instead, it is the combination of a relatively small number of quiescent luminous red objects due to the small area surveyed and the washing out of any red-sequence signal due to increasing color errors (see Figure 5(b)) that prevents us from detecting the red sequence beyond this redshift.

4.3. Evolution of the Color–Magnitude Relation

We use the error-weighted color histograms in thin redshift slices of $\Delta z \sim 0.1$ to track the color evolution of the peak in the red sequence and plot $(U_{280}–V)$ at the pivot point $M_V = -20$ in Figure 7. The color of the red-sequence peak is obtained with the MIDAS routine `CENTER/GAUSS gcursor`, which fits a Gaussian function to an emission line on top of a continuum. We mark the "continuum" level on both sides of the peak interactively, and obtain the peak location from the fit. We obtain errors from the uncertainty of the peak position obtained by varying the interval in which the Gaussian is being fit, but we do not include systematic calibration uncertainties in color (see Table 2 for results). We find that the $(U_{280}–V)_{M_V=-20}$ color of the peak evolves almost linearly with look-back time τ, and obtain a linear best fit (dashed line) of

$$(U_{280}–V)_{M_V=-20} = 2.57 - 0.195 \times \tau. \quad (4)$$

Our data points of the peak color scatter somewhat around this fit, which is an indication of our uncertainties in measuring the

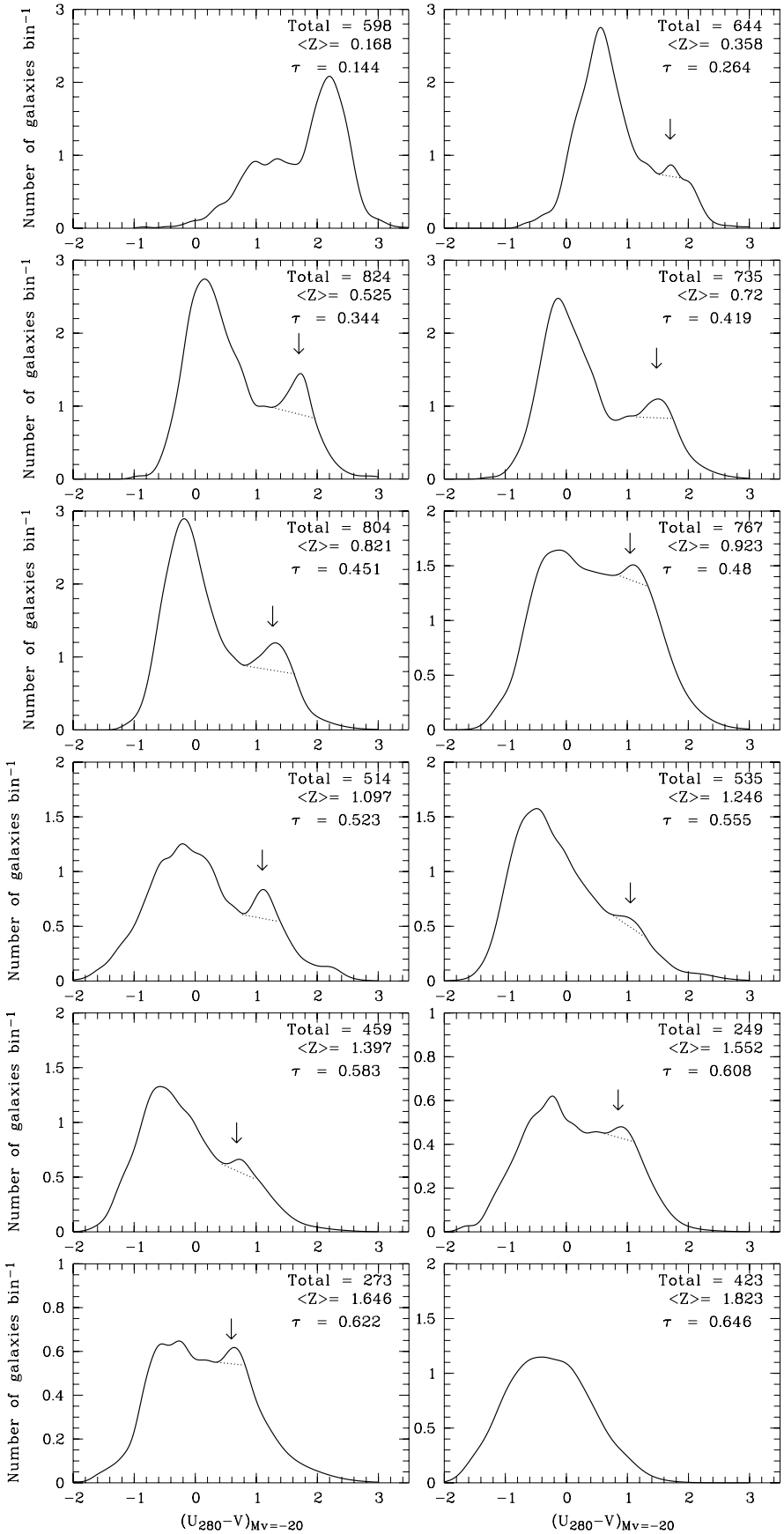

Figure 6. Rest-frame $(U_{280} - V)_{M_V=-20}$ galaxies color distribution in redshift slices. Histograms are sums of Gaussian probability distributions representing single galaxies with their individual color error. Structure is driven by bright objects with accurate colors while faint, large-error objects with broad, smooth distributions do not add contrast to the peaks. The top left panel contains the supercluster A901/2 with its prominent red sequence. The color of the red sequence peak, indicated by an arrow, is determined by a Gaussian fit to the localised excess above a continuum of galaxy counts. Thus, a red sequence is observed up to $z \simeq 1.6$. Number of galaxies, mean redshift and mean look-back time $\tau = z/(1+z)$ are noted.

Table 2
$(U_{280}-V)_{M_V=-20}$ Color of the Red-Sequence Peak

Mean Redshift	Redshift Interval	$(U_{280}-V)_{M_V=-20}$ (Vega mag)	$\delta\,(U_{280}-V)_{M_V=-20}$ (Vega mag)	Look-back Time (Gyr)
0.165	0.15−0.175	2.10	0.04	2.034
0.358	0.3−0.4	1.704	0.03	3.923
0.525	0.45−0.6	1.70	0.03	5.217
0.720	0.65−0.78	1.48	0.03	6.432
0.821	0.78−0.86	1.27	0.03	6.960
0.923	0.86−0.97	1.045	0.03	7.437
1.097	1.05−1.15	1.1	0.03	8.139
1.246	1.2−1.3	1.05	0.03	8.647
1.397	1.3−1.5	0.68	0.03	9.091
1.552	1.5−1.6	0.85	0.03	9.486
1.646	1.6−1.7	0.59	0.03	9.700

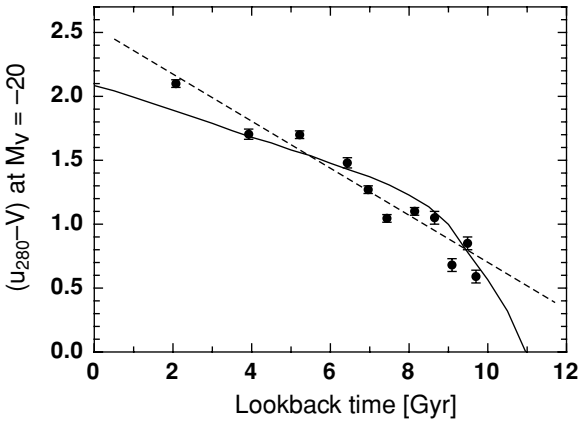

Figure 7. Evolution of the red-sequence color with look-back time $\tau = 15\mathrm{Gyr}\cdot z(1+z)^{-1}$, see Table 2. The dashed line is a linear fit to the points, and the solid line is an example prediction using PEGASE for a single age stellar population with solar metallicity formed 12 Gyr ago ($z_f = 3.7$). The error bars account only for the color measurement of the peak of the bright end of the red sequence. However, the scatter among the points illustrates further uncertainties including systematics and cosmic variance.

color, as any cosmological evolution of the average galaxy population is expected to be monotonic. However, these variations may also result from us looking at different environments at different redshift, which may be at different evolutionary stages, and not solely from our methodical uncertainties.

We obtain a CMR as a function of redshift using the approximation for the look-back time $\tau \simeq 15\mathrm{Gyr}\cdot z\cdot(1+z)^{-1}$, and separate blue and red galaxies with a parallel relation 0.47 mag bluer than the CMR, which is

$$(U_{280}-V)_{lim} = 2.10 - 0.3(M_V + 20) - 2.92z/(1+z). \quad (5)$$

In the low-redshift regime $0 < z < 1$ this cut is consistent with the one derived by Bell et al. (2004) considering an approximate color transformation derived from our templates, which is $(U-V) = 0.28 + 0.43(U_{280}-V)$. Our CMR is slightly steeper than the one derived by Bell et al. (2004), but that translates only into a minor color difference of <0.1 mag for galaxies in the relevant magnitude range $-24 < M_V < -18$. Although we see no clear red sequence at $z \gtrsim 1.65$, we extrapolate the CMR all the way up to $z = 2$ to isolate red galaxies across our entire sample.

The solid line in Figure 7 shows the evolution predicted by PEGASE for a single stellar population formed at a look-back time of 12 Gyr ($z_f = 3.7$) with solar metallicity. The bulk of our data are consistent with the pure aging model. Our lowest-redshift value is based entirely on the A901/2 supercluster at $z = 0.165$ (look-back time=2.0 Gyr), which is the highest-density environment in our sample.

5. EVOLUTION OF THE RED-SEQUENCE GALAXY POPULATION

We now focus on the color and the mass evolution of the whole red galaxy population, and analyze CMDs and color–stellar-mass diagrams (CM_*D) in redshift slices. We divide our galaxy sample into red and blue populations with the cut in Equation (5). Across the entire sample at $0 < z < 2$, roughly a third of the galaxies are red (3163 out of 10,692), but in the high-redshift part at $z > 1$ less than a quarter are red (843 out of 3479 galaxies).

5.1. Color–Magnitude Diagrams

The evolution of the red-sequence population is presented in the CMDs of Figure 8. In each panel, the solid line indicates the bimodality separation of Equation (5) assuming the mean redshift of the slice. The color of the data points shows their individual nature, and due to the width of the redshift intervals some galaxies scatter across the separating line. The top left panel in Figure 8 shows the CMD of the A901/2 supercluster centered at $z = 0.165$. Such a dense environment shows a clear red sequence, and this was used to derive the red-sequence slope in Equation (3). The red sequence is not as sharp and easy to visually distinguish on CMDs beyond $z = 1$, especially in the redshift slice $1.07 < z < 1.19$ due to the local increase in the scatter caused by large color uncertainties. This highlights the necessity of using error-weighted histograms to derive the CMR.

Altogether, we find that at a given magnitude both galaxy populations were bluer in the past, and in particular the bright end of the red sequence became ∼0.4 mag redder from $z = 2$ to $z = 0.2$. We also find an increasing population of bright ($M_V < -22$) blue ($(U_{280}-V) < 1$) galaxies at $z > 1$, which has also been reported by Taylor et al. (2009) in $(U-R)$ versus M_R CMDs of a K-selected sample at $0.2 < z < 1.8$ in the Extended Chandra Deep Field South.

5.2. Color–Stellar-mass Diagrams

Figure 9 shows the evolution of the population in CM_*D for the same redshift slices as the CMDs in Figure 8. We select the red sequence (black points) again with Equation (5). We reach smaller masses than Borch et al. (2006) because our galaxy sample is primarily H-band-selected instead of R-band-selected.

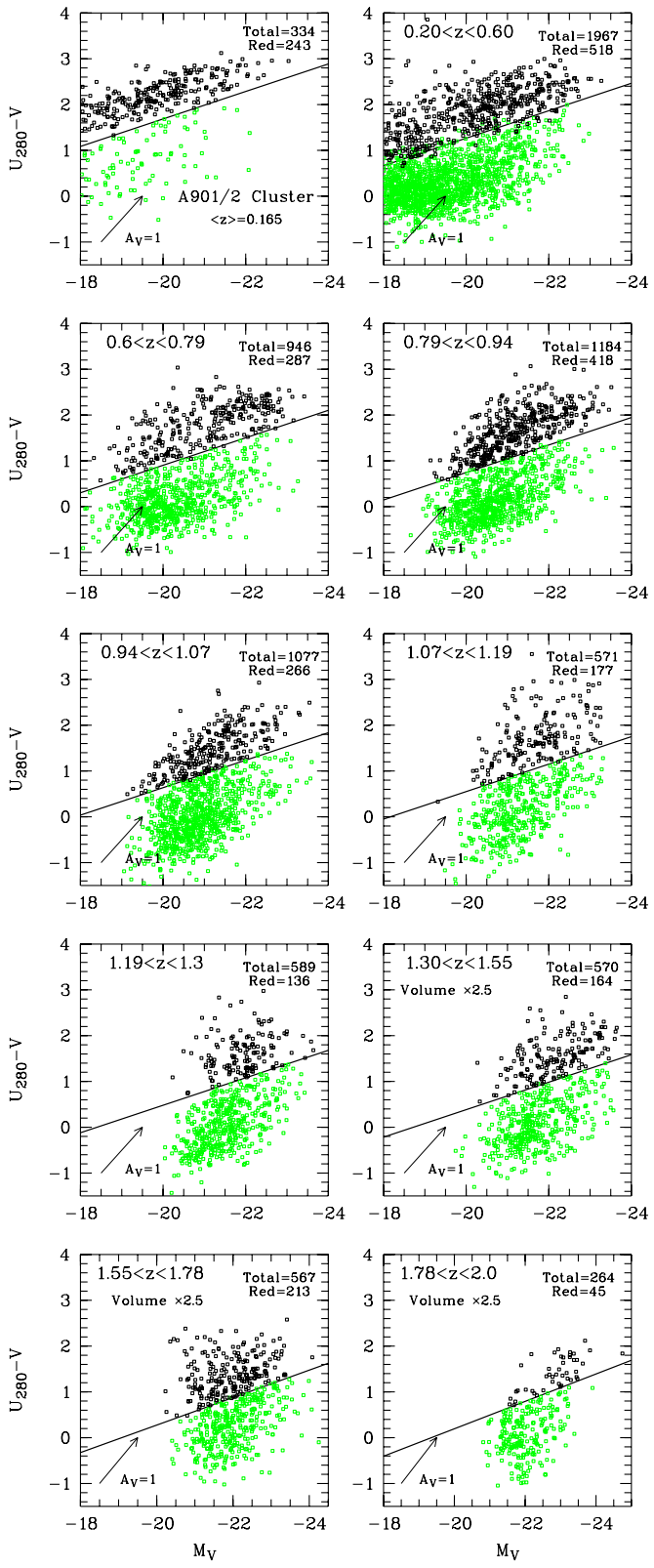

Figure 8. Color–magnitude diagrams in redshift slices. Solid lines indicate the bimodality separation (see Equation (5)) at the mean redshift of each bin. The real separation is given by the color of the data points (black: red sequence, green: blue cloud). The total number of galaxies and red fraction are noted. All redshift bins are nearly equal comoving volumes except for the three highest bins, which enclose 2.5 times as much volume, and the A901/2 cluster bin with a small volume enclosed within $0.150 < z < 0.175$. For reference, we show a reddening vector for $A_V = 1$ mag.

(A color version of this figure is available in the online journal.)

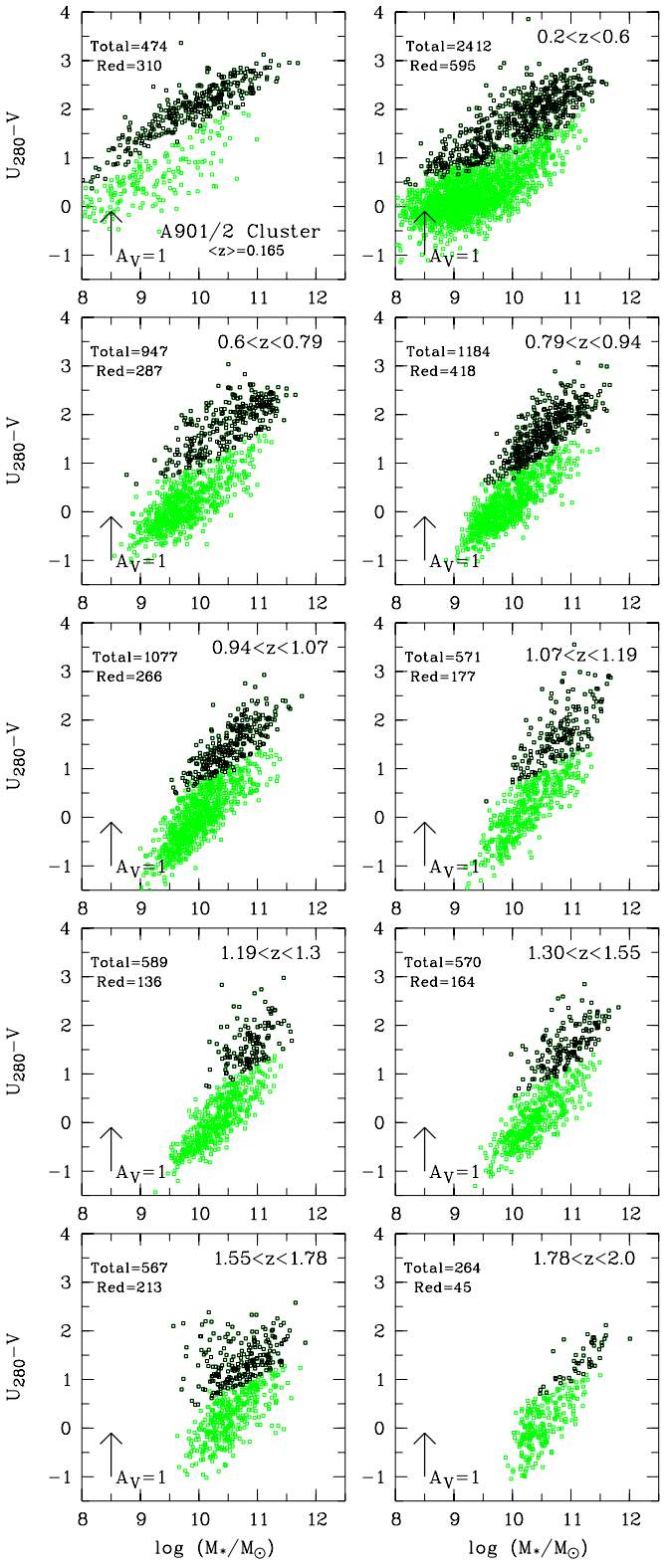

Figure 9. Color–mass diagrams in same redshift slices and format as Figure 8. The reddening vector assumes a Bell & deJong (2001) law for the stellar-mass–color relation and a Pei (1992) dust law.

(A color version of this figure is available in the online journal.)

Conversely, our blue galaxy population reaches less deep than that of Borch et al. (2006). We see a general trend whereby at fixed mass both galaxy populations were bluer in the past, just as they were at fixed magnitude. We find that massive galaxies

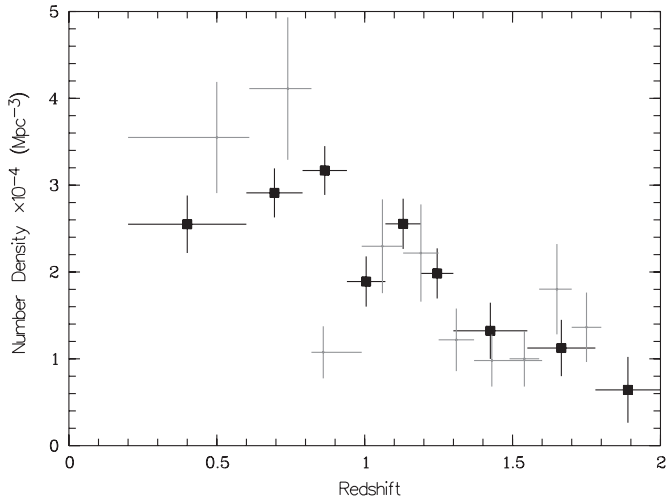

Figure 10. Number density evolution of massive red galaxies with $\log M_*/M_\odot > 11$ and $(U_{280}-V) > (U_{280}-V)_{lim}$ as a function of redshift. The error bars represent the cosmic variance in each redshift bin and were calculated with a method described by Moster et al. (2010). In gray, data from Taylor et al. (2009) for comparison.

between $0.2 \lesssim z \lesssim 1.0$ are dominated by the red population. This was also observed by Borch et al. (2006), who derived mass functions for the red and the blue galaxy population at $z < 1$ using the optical COMBO-17 data, and by many other authors (see, e.g., Bundy et al. 2005). However, at $z > 1$ there is a growing population of massive ($\log M_*/M_\odot \gtrsim 11$) blue ($(U_{280}-V) \lesssim 1$) galaxies as we go back in time, a phenomenon (also observed by Williams et al. 2009; Taylor et al. 2009) that has no analogue in the local universe.

The bottom right panel shows our highest redshift slice ($1.78 < z < 2$) where our sample contains 45 red galaxies. Among them are eight very massive ($\log M_*/M_\odot > 11.5$) objects, which means that at $z \sim 2$ the red sequence already contains very massive galaxies. The most massive object found in this high redshift slice has a stellar mass of $\log M_*/M_\odot = 12$. Our red sequence will contain dusty star-forming galaxies besides old galaxies, but since these do not form a sequence and are not focused in color, they will not affect the measurement of the red-sequence color with our tailored method.

5.3. Number Density Evolution of Massive Red Galaxies

Figure 10 shows the evolution of the number density of massive red galaxies as a function of redshift (see also Table 3). These red galaxies include both quiescent old galaxies as well as dust-reddened galaxies. We avoid the supercluster A901/2 by constraining our sample to $0.2 < z < 2$ and choose masses of $\log M_*/M_\odot > 11$, where we are complete at all redshifts, thus retaining only 478 objects.

We find that the number density of massive red galaxies rises considerably (by a factor ∼4) from $z \sim 2$ to $z \sim 1$ and is more or less constant at $z < 1$. Due to the small survey area our results are affected by cosmic variance on the order of 30% as estimated using Moster et al. (2010). Nevertheless, our results are comparable within the error bars to results by the GOODS-MUSIC survey (0.04 deg^2 area) (Fontana et al. 2006) and the MUSYC survey (0.6 deg^2 area) (Taylor et al. 2009). In the highest redshift bin at $z \sim 2$, the number density derived is consistent with the spectroscopic survey of Kriek et al. (2008). Since any sample of red galaxies could in principle be contaminated by some dusty red galaxies the number density

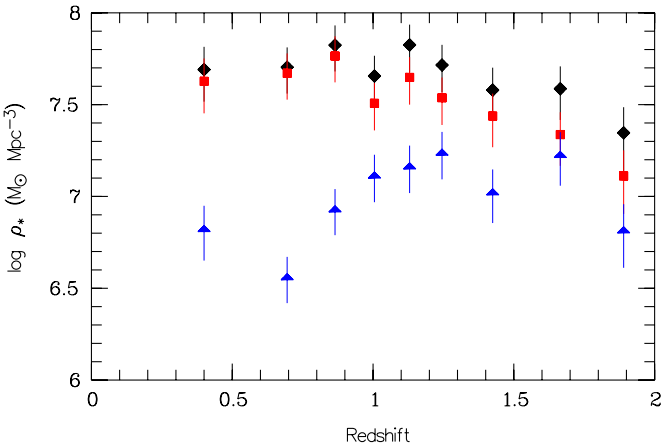

Figure 11. Stellar mass density evolution of galaxies with $\log M_*/M_\odot > 11$ as a function of redshift. The entire galaxy population (diamond) is divided into the red-sequence (square) and blue-cloud galaxy population (triangle). Error bars include only cosmic variance estimates and no uncertainty from the stellar mass estimation.

(A color version of this figure is available in the online journal.)

Table 3
Number and Stellar Mass Density of Galaxies with $\log M_*/M_\odot > 11$

Redshift Interval	$\phi_{\rm red}$ (10^{-4} Mpc^{-3})	$\log \rho_{*_{\rm red}}$ ($M_\odot$ Mpc^{-3})	$\log \rho_{*_{\rm blue}}$ ($M_\odot$ Mpc^{-3})	$\log \rho_{*_{\rm all}}$ ($M_\odot$ Mpc^{-3})
0.2−0.6	2.550	7.627	6.825	7.691
0.6−0.79	2.911	7.671	6.563	7.704
0.79−0.94	3.169	7.765	6.932	7.824
0.94−1.07	1.890	7.508	7.117	7.656
1.07−1.19	2.555	7.648	7.167	7.825
1.19−1.3	1.984	7.538	7.241	7.716
1.3−1.55	1.323	7.438	7.025	7.579
1.55−1.78	1.125	7.337	7.229	7.586
1.78−2.0	0.643	7.112	6.818	7.346

derived here represents an upper limit. However, we do not expect the effect to be large at the high-mass end.

5.4. Stellar-mass Density Evolution of Massive Galaxies

The different evolution of stellar mass density in red and blue galaxies is shown in Figure 11 (see also Table 3). Again we restrict ourselves to masses of $\log M_*/M_\odot > 11$, where we are complete across $0.2 < z < 2$. Like the number density, the stellar mass density of the red population increases by a factor of ∼4 from $z \sim 2$ to $z \sim 1$ and remains roughly constant at lower redshifts. In contrast, the stellar mass density of the blue population increases only by a factor of ∼2 from $z \sim 2$ to $z \sim 1.2$ and decreases by the same factor toward low redshift again. Altogether, the overall stellar mass density increases by a factor of ∼3 from $z \sim 2$ to $z \sim 1$ due to the combined contribution of red and blue galaxies, while it remains constant at lower redshift where the red sequence dominates. Thus, the main formation epoch of the massive red galaxy population is ranges over $2 > z > 1$.

Comparing our stellar mass densities with the literature is not foolproof since different surveys have different selection criteria using, e.g., color, morphological types and star formation activity. They employ different methods to derive the stellar mass and they can be affected by cosmic variance.

Our results for the evolution of the mass density of the entire population between $1 > z > 0$ are consistent with Conselice et al. (2007) who also found little evolution for galaxies with $11 < \log M_*/M_\odot < 11.5$. At higher redshift, our results differ:

Conselice et al. (2007) found an increases by a factor 10.7 from $z \sim 2$ to $z \sim 1$, while our results show a more modest rise by a factor ∼3.

Based on a 3.6 μ selected sample of galaxies Arnouts et al. (2007) found an increase of the mass density in the quiescent population by a factor of 2 from $z \sim 1.2$ to $z \sim 0$, while the star-forming population shows no evolution. Additionally, at higher redshift between $2 > z > 1.2$ they found that the quiescent population increases by a factor of 10 while the star formation population increases by a factor of 2.5. However, these results are based on a magnitude-selected sample and not a mass-selected one.

Cirasuolo et al. (2007) found in a sample of $M_k \leqslant -23$ galaxies that the space density of bright red galaxies is nearly constant over $1.5 \gtrsim z \gtrsim 0.5$, while that of bright blue galaxies decreases by a factor of ∼2 over the same redshift interval.

Recently, Ilbert et al. (2010) found a rise in the stellar mass density of $\log M_*/M_\odot > 11$ galaxies from $z \sim 2$ to $z \sim 1$ by a factor ∼14 for quiescent galaxies and a factor of ∼4.3 for red-sequence galaxies, similar to our result. This difference between quiescent and red-sequence galaxies is likely to arise from red star-forming galaxies that contaminate the red sequence more toward $z \sim 2$. For both quiescent and red-sequence galaxies, they found little evolution at $z < 1$, as we do. Also, their highly star-forming sample compares well to our blue galaxy population. They find a rise in mass density by a factor of ∼1.5 from $z \sim 2$ to $z \sim 1$ and a decrease by a factor of ∼2.5 at lower redshift again.

6. SUMMARY AND CONCLUSION

In this work we investigated the evolution of the red sequence in terms of color, luminosity, mass, and number density through cosmic time since $z = 2$. We derived an H-band catalog of 10,692 galaxies from 0.2 deg^2 of the A901-field surveyed by the deep NIR multi-wavelength survey COMBO-17+4. While deep multi-wavelength surveys provide photometric redshifts for large samples of galaxies, the measured colors suffer from large uncertainties at high redshift that wash out the contrast with which the red sequence appears on top of the tail extending from the blue cloud. Hence, we used color histograms weighted by the color error of each galaxy to trace even a diluted red-sequence signal. We also used the rest-frame color (U_{280}–V) for maximum population contrast and minimum sensitivity to redshift errors.

As a result, we found a red sequence up to $z \sim 1.65$, beyond which the situation is unclear. Tracking the color evolution of the red-sequence peak, we derived an evolving CMR up to $z = 2$ and used it to separate the red and blue galaxy populations. Our results show that the (U_{280}–V) color evolution of the red sequence is consistent with pure aging. Further results are the following.

1. Both the red and blue galaxy population get redder by $\Delta(U_{280}$–$V) \sim 0.4$ mag since $z = 2$.
2. The population of massive blue galaxies grows from $z \sim 1$ to $z \sim 2$.
3. The massive end of CM$_*$Ds is dominated by the red galaxy population at $z < 1$ and by both galaxy populations at $z > 1$.
4. Some massive red galaxies with $\log M_*/M_\odot \sim 11.5$ are already in place at $z \sim 2$.

We investigated the number density and stellar mass density evolution of massive red galaxies and found that both increase by a factor ∼4 between $2 > z > 1$ and shows little evolution since $z = 1$. This suggests that the main formation epoch of massive red galaxies is at $2 > z > 1$ such that they have assembled most of their mass by $z \sim 1$. Note, that our masses are unlikely to be biased much by dust.

It is clear that our results are affected by cosmic variance due to the small area surveyed. Once the data are available from the two other fields (A226 and S11) targeted by the COMBO-17+4 survey, we expect to create an H-band-selected catalog of ∼50,000 galaxies in an area of 0.7 deg^2, of which ∼12,000 galaxies will be above $z = 1$. The more than threefold increase in area and the combination of unrelated fields on the sky will reduce the effect of cosmic variance by a factor three and firm up our findings quantitatively.

We are grateful to all Calar Alto staff astronomers, in particular Jesus Aceituno, Anna Guijaro, Felipe Hoyo, and Ulli Thiele. Thanks to the International Max-Planck Research School for fundings. C.W. was supported by an STFC Advanced Fellowship.

REFERENCES

Arnouts, S., et al. 2007, A&A, 476, 137
Bell, E. F., & de Jong, R. S. 2001, ApJ, 550, 212
Bell, E. F., et al. 2004, ApJ, 608, 752
Bertin, E., & Arnouts, S. 1996, A&AS, 117, 393
Borch, A., et al. 2006, A&A, 453, 869
Bundy, K., Ellis, S. R., & Conselice, C. 2005, ApJ, 625, 632
Cassata, P., et al. 2008, A&A, 483, L39
Cimatti, A., et al. 2004, Nature, 430, 184
Cirasuolo, M., et al. 2007, MNRAS, 380, 585
Conselice, C. J., et al. 2007, MNRAS, 381, 962
Daddi, E., et al. 2005, ApJ, 626, 680
Falter, S., et al. 2010, A&A, submitted
Faßbender, R. 2003, Diploma thesis, Univ. Heidelberg
Fioc, M., & Rocca-Volmerange, B. 1997, A&A, 326, 950
Fontana, A., et al. 2006, A&A, 459, 745
Franzetti, P., et al. 2007, A&A, 465, 711
Glazebrook, K., et al. 2004, Nature, 430, 181
Gray, M. E., et al. 2009, MNRAS, 393, 1275
Ilbert, O., et al. 2010, ApJ, 709, 644
Kriek, M., van der Wel, A., van Dokkum, P. G., Franx, M., & Illingworth, G. D. 2008, ApJ, 682, 896
McGrath, E. J., Stockton, A., & Canalizo, G. 2007, ApJ, 669, 241
Moster, B., Somerville, R. S., Newman, J. A., & Rix, H.-W. 2010, ApJ, submitted
Pei, Y. C. 1992, ApJ, 395, 130
Pickles, A. J. 1998, PASP, 110, 863
Röser, H.-J., & Meisenheimer, K. 1991, A&A, 252, 458
Simon, P., et al. 2010, MNRAS, submitted
Taylor, A. N., et al. 2004, MNRAS, 353, 1176
Taylor, E. N., et al. 2009, ApJ, 694, 1171
Tody, D. 1993, in ASP Conf. Ser. 52, Astronomical Data Analysis Software and Systems II, ed. R. J. Hanisch, R. J. V. Brissenden, & J. Barnes (San Francisco, CA: ASP), 173
Weiner, B. J., et al. 2005, ApJ, 620, 595
Williams, R. J., Quadri, R. F., Franx, M., van Dokkum, P., & Labbé, I. 2009, ApJ, 691, 1879
Wolf, C. 1998, PhD thesis, Univ. Heidelberg
Wolf, C., Meisenheimer, K., & Gray, M. E. 2005, A&A, 443, 435
Wolf, C., Meisenheimer, K., Rix, H-W., Borch, A., Dye, S., & Kleinheinrich, M. 2003, A&A, 401, 73
Wolf, C., et al. 2001, A&A, 365, 681
Wolf, C., et al. 2004, A&A, 421, 913
Wolf, C., et al. 2009, MNRAS, 393, 1302